Effects of fluvial sedimentary heterogeneity on CO_2 geological storage: Integrating storage capacity, injectivity, distribution and CO_2 phases

Xiaolong Sun[a,b*], Yingchang Cao[a,b*], Keyu Liu[a,b], Juan Alcalde[c], Patricia Cabello[d,e], Anna Travé[f,e], David Cruset[c], Enrique Gomez-Rivas[f,e]

[a] School of Geosciences, China University of Petroleum (East China), Qingdao 266580, China

[b] Shandong Provincial Key Laboratory of Deep Oil and Gas, Qingdao 266580, China

[c] Geosciences Barcelona (GEO3BCN-CSIC), Barcelona 08028, Spain

[d] Departament de Dinàmica de la Terra i de l'Oceà, Facultat de Ciències de la Terra, Universitat de Barcelona (UB), Barcelona 08028, Spain

[e] UB-Geomodels Research Institute, Universitat de Barcelona (UB), Barcelona 08028, Spain

[f] Departament de Mineralogia, Petrologia i Geologia Aplicada, Facultat de Ciències de la Terra, Universitat de Barcelona (UB), Barcelona 08028, Spain

This is a postprint version of this article:

Sun, X., Cao, Y., Liu, K., Alcalde, J., Cabello, P., Travé, A., Yuan, G., Cruset, D., and Gomez-Rivas, E. 2023. Effects of fluvial sedimentary heterogeneity on CO_2 geological storage: integrating storage capacity, injectivity, distribution and CO_2 phases. *Journal of Hydrology*, 617(A), 128936. DOI: https://doi.org/10.1016/j.jhydrol.2022.128936

The published copy-edited version can be found at:

https://www.sciencedirect.com/science/article/abs/pii/S0022169422015062

Abstract: Fluvial system deposits often form suitable reservoirs for CO_2 geological storage (CGS). These potential storage sites usually present heterogeneous fluvial architectures at multiple scales. This heterogeneity can exert varied effects on different aspects of CGS, resulting in significant storage efficiency variability. Here, we investigate the effects of variable fluvial lithofacies associations on CO_2 storage, using the Puig-reig anticline in the SE Pyrenees (Spain) as a reservoir analog. To test this, we employ a multidisciplinary approach that integrates field sedimentology, reservoir modeling, and numerical simulation of CO_2 injection to produce models akin to different fluvial lithofacies associations. The storage volume and injectivity of CO_2 are found to decrease in reservoirs with decreasing fractions and sizes of high-permeable facies from the proximal to the medial-distal lithofacies associations. The flow barriers created by low-permeable facies can hinder the vertical migration of the CO_2 plume and prevent it from reaching the reservoir top, hence reducing the direct contact between the CO_2 plume and the overlying caprock. Furthermore, an

optimal amount of low-permeable layers (around 30% in this study) can increase the swept area of CO_2 and reduce the proportions of free CO_2 phase. These aspects can collectively increase the amount of permanently trapped CO_2 and reduce the leakage risks of the injected CO_2. Based on the characteristics of the resulting models (i.e., storage volume, injectivity, distribution and phases of CO_2), a multi-criteria decision-making method has been used to quantitatively rank the different lithofacies associations according to their suitability for CO_2 storage. In this analysis, the proximal-medial fluvial lithofacies associations are assessed to be the most suitable ones because they feature low proportions of the injected CO_2 reaching the reservoir top and in free phase while maintaining the high storage volume and injectivity. This study reveals that heterogeneous reservoir architectures appear to have mixed effects on CO_2 storage, and reservoirs featuring moderately heterogeneous architectures (appropriate fractions of low-permeable facies ranging from 30% to 40%) are beneficial to keeping the balance among different aspects of CO_2 storage. This provides new insights for the screening and selection of potential geological sites for CO_2 storage.
Keywords: CO_2 geological storage, trapping mechanism, reservoir heterogeneity, fluvial lithofacies association.

1. Introduction

To date, 194 parties have submitted their Nationally Determined Contributions (NDC) to the Paris Agreement to describe their strategies for climate change mitigation (UNFCCC, 2022). Among these, more than forty countries mention carbon capture and storage (CCS) explicitly in their national climate change mitigation pathways (Sun et al., 2021a). Although CCS has been widely considered an important technology for greenhouse gas reduction (Alcalde et al., 2018; Bui et al., 2018; IPCC, 2018), particularly to decarbonize industrial emissions, there is a huge gap between the current global CCS deployment and that which will be ultimately required to achieve the global mitigation targets (Global CCS Institute, 2018; Sun et al., 2020). CCS deployment has stalled in most countries due to various barriers (Scott et al., 2013), such as a high development cost perception, lack of market mechanisms and incentives, potential safety and environmental issues (Leung et al., 2014; Budinis et al., 2018; Alcalde et al., 2019; Tcvetkov et al., 2019), and low public acceptance (Seigo et al., 2014; Witte, 2021). Ensuring the safety and efficiency of the CO_2 geological storage (CGS) operations is essential to make CCS commercially and environmentally sustainable and socially acceptable.

Once the captured CO_2 is injected into a geological reservoir, different trapping mechanisms (i.e., structural, residual, dissolution and mineralization trapping) act on it at different rates to keep the CO_2 trapped in the subsurface (Bachu et al., 2007; Shukla et al., 2010; De Silva and Ranjith, 2012). Structural trapping dominates the early storage stage (first decades), and depends on the caprock integrity to resist the injection pressure during the injection stage and the buoyancy pressure in the early post-injection period (Shukla et al., 2010; Espinoza and Santamarina, 2017; Iglauer, 2018). The other trapping mechanisms do not rely on caprock efficiency, but on the physical-chemical interactions between fluids and/or rocks. These mechanisms are controlled by various factors, including temperature, pressure, fluid and rock compositions, wettability, and pore structure, among others (Riaz and Cinar, 2014; Raza et al., 2015; Romanov et al., 2015). Mineralization trapping is considered the safest mechanism, but its action is limited in most candidate reservoirs even after thousands of years, except in reservoirs with sufficient divalent cation-bearing minerals and rapid dissolution rates of these minerals (Zhang et al., 2013; Zhang and DePaolo, 2017). Under these circumstances, capillary trapping and dissolution trapping mechanisms play a critical role in ensuring storage security in the short-medium term (tens to hundreds of years).

Apart from engineering factors, such as the combination of injected fluids, injection rate, and well configuration (Raza et al., 2015; Al-Khdheeawi et al., 2017a, 2018; Ren and Jeong, 2018), the geological characteristics of the reservoir determine CO_2 trapping efficiency. For instance, heterogeneous fluvial architectures (lithofacies and their associations) not only control the CO_2 storage capacity and injectivity (Ambrose et al., 2008; Issautier et al., 2014, 2016) but also the spatial distribution and fractions of different CO_2 phases (Gershenzon et al., 2015; Ershadnia et al., 2021, 2022). Previous studies suggest that most regions have sufficient geological storage capacity for CO_2 (Kearns et al., 2017; Ringrose and Meckel, 2019; Sun et al., 2020), indicating that it seems not to be a limiting factor for CGS deployment. However, having a high storage capacity is still a primary requirement in the selection of suitable sites. Sufficient storage capacity helps to guarantee that the selected storage site is economically viable by reducing the unit cost while more stored CO_2 shares similar capital costs, i.e., the economy of scale (Alcalde et al., 2019, 2021). The presence of low porosity and permeability deposits within the target reservoir (e.g., in the form of overbank deposits in fluvial systems) can reduce the storage capacity and thus the trapping efficiency. Furthermore, with the increasing fraction of these flow barriers, the overall reservoir (mainly channel deposits) quality and connectivity deteriorate. This results in decreasing reservoir injectivity, such as a lower injection rate at a given injection pressure or a higher injection pressure at a constant injection rate. Excessive injection pressure can potentially damage the well (Bai et al., 2016; Gholami et al., 2021) and rock integrity (Rutqvist et al., 2008; Li et al., 2022), thus resulting in leakage risk.

Heterogeneous deposits can also create asymmetric distributions of the injected CO_2 (Xu et al., 2020; Kou et al., 2021). The different lithofacies forming a heterogeneous reservoir may present varying capillary pressure values, which can locally produce areas of enhanced capillary trapping. These areas may develop larger gas saturation than the residual gas saturation (Saadatpoor et al., 2010; Krevor et al., 2011), and can prevent CO_2 migration towards the caprock. The larger this contrast in capillary pressure is, the larger the proportion of local capillary trapping can be produced (Gershenzon et al., 2017c). However, local capillary trapping can partially fail to retain the CO_2 in the reservoir due to the accumulated buoyancy forces acting on the CO_2 plume, or completely fail due to rock fracturing. The influence of fluvial stratigraphic architectures on residual and dissolution trapping mechanisms has been extensively investigated (Gershenzon et al., 2015). For example, due to the heterogeneous relative permeability in different lithofacies, a small amount of residual trapping occurs during the injection stage, in addition to the large proportion existing in the post-injection period (Gershenzon et al., 2017b). Compared to relatively homogeneous reservoirs, dominated by the vertical migration of the CO_2 plume with limited lateral migration, the CO_2 plume in heterogeneous reservoirs can propagate farther in the horizontal direction due to the existence of low-permeable layers in the vertical direction. This can result in a larger contact area between the CO_2 plume and the pore-filling brine, leading to a larger ratio of dissolution trapping (Gershenzon et al., 2015, 2016). Larger contrast in permeability between different rock types can increase the volume of the CO_2 plume, increasing the efficiency of dissolution and residual trapping mechanisms (Gershenzon et al., 2017c). This prevents the CO_2 plume migration to caprocks or surfaces and thus reduces the risk of CO_2 leakage. However, reservoir heterogeneity can also produce other effects on the storage performance, such as a reduction in sweep efficiency of the CO_2 plume produced by low-permeable units (Yang et al., 2020). Although the reservoir heterogeneity enhances the lateral flow of the CO_2 plume, it also inhibits the vertical migration of CO_2. Thus, the effects of reservoir heterogeneity on CO_2 plume migration and CO_2 phases depend on the specific reservoir structure. An overall decreasing sweep efficiency of CO_2 plume caused by a high fraction of flow barriers can also reduce the efficiency of residual trapping (Han et al., 2010) and dissolution trapping (Al-Khdheeawi et al., 2017b).

In summary, heterogeneous reservoir architectures exert significant but varied effects on different aspects of CO_2 storage. Compared to relatively homogeneous reservoirs, heterogeneous reservoir architectures generally feature lower storage capacity and injectivity for CO_2. However, under certain circumstances, the presence of low-permeable layers can hinder the vertical migration of the CO_2 plume and reduce the fraction of free CO_2 in the pores, which can reduce the risk of CO_2 leakage. It is still controversial whether heterogeneous reservoir architectures can enhance the overall efficiency of CO_2 storage. In this study, we use the Puig-reig anticline, in the SE Pyrenees (Spain), as a heterogeneous fluvial reservoir analog. Based on the previous field studies on outcrop sedimentology and reservoir characteristics (Cruset et al., 2016; Sun et al., 2021b, 2021c, 2022), we summarize the sedimentary and reservoir characteristics of typical lithofacies associations. Through systematic reservoir modeling and numerical simulating, this study aims to determine the overall effects of different fluvial lithofacies associations on the efficiency of CO_2 storage based on a comprehensive consideration of storage capacity, injectivity, distribution and phases of CO_2.

2. Sedimentology background

The Puig-reig anticline is located in the SE Pyrenean fold and thrust belt (Spain) (Fig. 1A), and developed along the footwall of the frontal Vallfogona thrust emplaced over the Ebro Foreland Basin (Fig. 1B) (Vergés, 1993). This anticline is a km-scale gentle anticline with a flat hinge. Its upper part is characterized by the Berga Group and the Solsona Formation deposited from alluvial-fluvial systems during the Late Eocene and the Oligocene (Williams et al., 1998; Barrier et al., 2010). This study focuses on the well-exposed and well-preserved outcrops of the Middle Berga Group and the Solsona Formation along several roads in the Puig-reig anticline (Fig. 1C, D). These sequences were interpreted as the result of sedimentation in a proximal to medial fluvial system, and present gradual changes of lithofacies associations from the foreland basin margin inwards (Sun et al., 2021b). The proximal fluvial lithofacies associations (LAp) represent sedimentary environments of unconfined flash floods and wide-shallow channel streams, and are characterized by major conglomerates and minor coarse-medium sandstones with limited fine deposits (Fig. 2A, B). The medial fluvial deposits represent sedimentary environments of channel streams and overbank areas, and include the proximal-medial fluvial lithofacies associations (LApm) and the medial-distal fluvial lithofacies associations (LAmd). The LApm is characterized by interbedded conglomerates, coarse-medium sandstones, and fine deposits (Fig. 2C, D). The LAmd consists of coarse-medium sandstones and more fine deposits (Fig. 2E, F). The distal fluvial deposits (LAd) are located southward of our study area, and are composed of terminal lobes or fluvial-dominated deltas and interdistributary bays (Sáez et al., 2007).

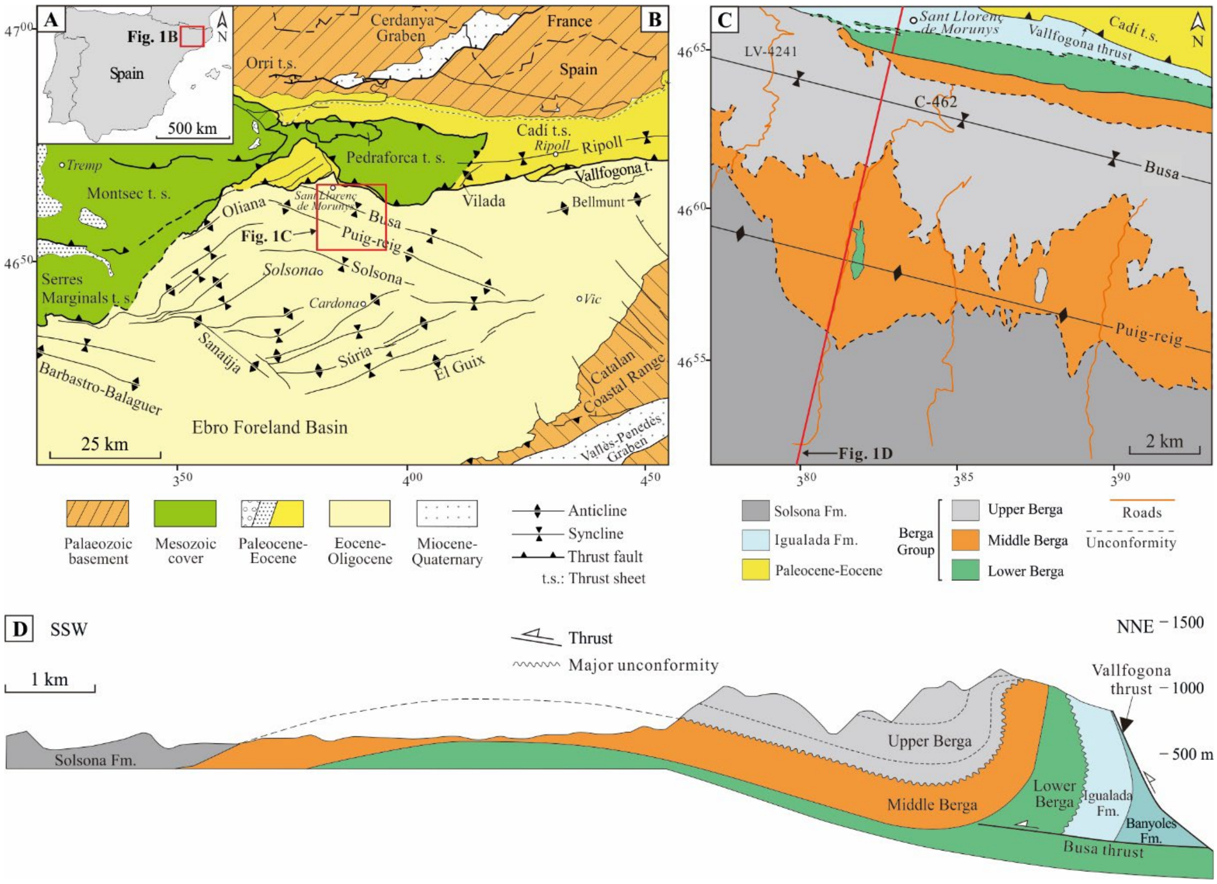

Fig. 1. (A-B) Geographical location and main structural units of the SE Pyrenean fold-and-thrust belt and the Ebro Foreland Basin (Vergés, 1993). (C-D) Distribution of the Berga Group and the Solsona Formation. Fig. 1D is modified from Williams et al. (1998) and Barrier et al. (2010).

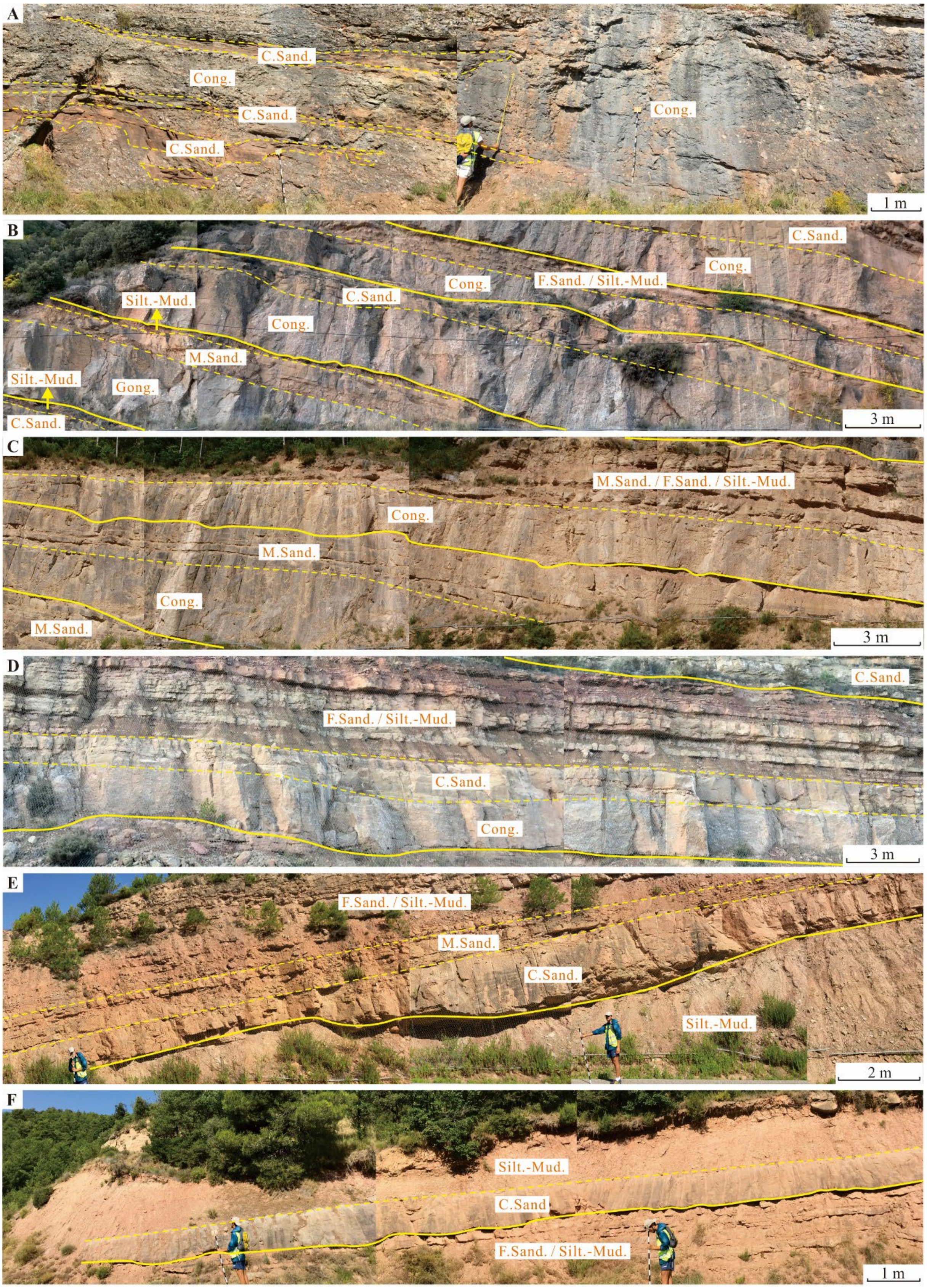

Fig. 2. Field photos of typical lithofacies associations in the Puig-reig anticline, modified from Sun et al. (2021b): (A-B) proximal fluvial lithofacies associations (LAp); (C-D) proximal-medial fluvial lithofacies associations

(LApm); (E-F) medial-distal fluvial lithofacies associations (LAmd) (Cong.: conglomerate; C.Sand.: coarse sandstone; M.Sand.: medium sandstone; F.Sand.: fine sandstone; Silt.: siltstone; Mud.: mudstone).

3. Methodology

3.1. Reservoir modeling

Reservoir models have been built using the Petrel E&P Software Platform (by Schlumberger). The three-dimensional model size is 5000 m×5000 m×50 m, with 125,000 cells with a size of 100 m×100 m×1 m each. For each lithofacies association, lithofacies have been grouped in the lower high-permeable facies of fluvial channel deposits and the upper low-permeable facies of overbank deposits. High-permeable facies consist of conglomerates and coarse-medium sandstones, and low-permeable facies consist of mudstones, siltstones, and fine sandstones. The fractions and thicknesses of high-permeable facies were measured from the studied outcrops. The LAp is generally characterized by a high fraction (⩾80%) and large thickness (⩾8 m) of high-permeable facies. Compared to the LAp, the LApm features a lower fraction and smaller thickness of high-permeable facies. The LAmd is generally characterized by a relatively low fraction (⩽40%) and small thickness (⩽4 m) of high-permeable facies. To represent the gradual changes of geometric characteristics from proximal to distal fluvial lithofacies associations, ideal model scenarios were designed with regularly decreasing fractions and thickness of high-permeable facies (Table 1). The width/thickness ratio of high-permeable facies was assigned as a constant value of 100 to represent general fluvial channels (Gibling, 2006). The channel tortuosity, defined as the ratio of the channel length to the direct axial length, was assigned gradually increasing values from 1.08 to 1.40 to represent the generally increasing channel tortuosity from proximal to distal fluvial systems (Friend and Sinha, 1993). In total, 11 model scenarios were designed, with model scenarios 1 to 3, 4 to 6, and 7 to 9 representing the LAp, LApm, and LAmd of the Puig-reig anticline, respectively, and scenarios 10 and 11 representing the LAd outside this anticline.

For each model scenario, a facies model was created using the object modeling algorithm based on the geometric characteristics of different facies. This method can create a stochastic facies model and present the representative geometric characteristics of reservoirs, especially fluvial channels. The fluvial channel object was used as the high-permeable facies using the aforementioned geometric parameters. Because all sediments have been grouped into two categories of facies, the low-permeable facies was set as the background object to fill the remaining model space between the fluvial channel objects. Abundant fractures, developed in these fluvial deposits in the Puig-reig anticline (Sun et al., 2021c), were not included in the subsequent petrophysical modeling because it is out of the scope of this study, focusing on the effects of different fluvial lithofacies associations on CO_2 storage. For each facies model, a porosity model was created using the Gaussian random function algorithm, because this method can create a facies-controlled porosity model constrained by the geometric characteristics of the high-permeable and low-permeable facies. For all model scenarios, theoretical porosity ranges were set as 0.2 to 0.3 for high-permeable facies and 0.1 to 0.2 for low-permeable facies. These porosity ranges can represent relatively high-quality reservoirs, which are the prior targets for CGS at the present stage due to their larger storage capacity and higher injectivity than low-porosity reservoirs. Permeability *(k)* and irreducible water saturation *(S_{wi})* were calculated using the empirical formulas proposed by Holtz (Holtz, 2002), which have been widely used and proved to be effective for CO_2 storage simulation in fluvial sequences by previous studies (Gershenzon et al., 2015, 2016, 2017c; Ershadnia et al., 2021). Horizontal permeability was calculated from porosity (Φ) using the empirical formula (Holtz, 2002), while vertical permeability was calculated based on a ratio of vertical k to horizontal k of 0.2 to represent the permeability anisotropy in sedimentary rocks:

$$k=7\times 10^{7}\times \Phi^{9.61} \quad (1)$$

Based on the average porosity and permeability, the average S_{wi} was calculated using the empirical formula (Holtz, 2002) for high-permeable and low-permeable facies, respectively (Table 2):

$$S_{wi}=5.159\times \left(\frac{\log k}{\Phi}\right)^{-1.559} \quad (2)$$

The ratio (R) of the theoretical storage volume (V_r) to the total rock volume (V_t) of each model scenario was calculated using a volumetric method:

$$R=\frac{V_r}{V_t}=\Phi\times(1-S_{wi}) \quad (3)$$

Table 1 Key geometric parameters used for facies modeling.

Model scenarios		High-permeable facies: fluvial channels				Low-permeable facies: overbank deposits	
		Fraction (%)	Thickness (m)	Width (m)	Channel sinuosity	Fraction (%)	Geometric
	1	100	/	/	/	0	Background facies
LAp	2	90	9	900	1.08	10	
	3	80	8	800	1.12	20	
	4	70	7	700	1.16	30	
LApm	5	60	6	600	1.20	40	
	6	50	5	500	1.24	50	
	7	40	4	400	1.28	60	
LAmd	8	30	3	300	1.32	70	
	9	20	2	200	1.36	80	
LAd	10	10	1	100	1.40	90	
	11	0	/	/	/	100	

3.2. Numerical simulation of CO_2 storage

Reservoir simulations of 11 model scenarios were carried out using the Eclipse 300 numerical simulator (by Schlumberger) with the CO2STORE option. Eclipse 300 is fully compatible with Petrel, and it is a multidimensional compositional simulator with a cubic equation of state, pressure-dependent permeability, or black oil fluid treatment (Class et al., 2009; Schlumberger, 2018). Its CO2STORE option can simulate different CGS processes and consider free, residual and dissolved CO_2 phases, which have been widely used in CO_2 injection simulation in previous studies (Gershenzon et al., 2015, 2016, 2017b; Abbaszadeh et al., 2020). These CO_2 phases represent the main CO_2 trapping mechanisms acting in the relatively short-medium period (injection stage to a few hundred years), and determine whether the injected CO_2 will remain within the reservoir for subsequent mineralization trapping in the longer term. Based on different model scenarios, reservoir simulations in this study aim to determine the overall effects of different lithofacies associations on the injectivity, distribution and CO_2 phases. The key parameters for reservoir simulations are summarized in Table 2. Considering the distinct physical properties of the high-permeable and low-permeable facies, different relative permeability curves and capillary pressure curves were used (Fig. 3). The facies-based curves were used rather than totally scaled cell-based curves, because the latter situation will significantly increase simulation time to be impractical for these large 3D models. Based on the average porosity of each facies, the maximum residual gas saturation (S_{gr-max}) was calculated using the empirical formula proposed by Holtz (Holtz, 2002), which has been widely used in previous studies on CO_2 storage (Gershenzon et al., 2015, 2016, 2017c; Ershadnia et al., 2021):

$$S_{gr-max}=-0.969\times\Phi+0.5473 \quad (4)$$

For relative permeability, the Brooks-Corey relation in the form proposed by Dullien (Dullien, 1992) was used to calculate the relative permeability curves:

$$K_{rw}=\left(\frac{S-S_{wi}}{1-S_{wi}}\right)^{N_w} \quad (5)$$

$$K_{rg}=K_{rg}(S_{wi})\left(1-\frac{S-S_{wi}}{1-S_{gr}-S_{wi}}\right)^{2}\left(1-\left(\frac{S-S_{wi}}{1-S_{gr}-S_{wi}}\right)^{N_g}\right) \quad (6)$$

where S is the water saturation. N_w and N_g are the pore-size distribution index for water and CO_2, and were assigned values of 5 and 4, respectively, following Krevor et al. (Krevor et al., 2012). $K_{rg}(S_{wi})$ is the maximum gas relative permeability when S is equal to S_{wi}, and was assigned values of 0.95 and 0.65 for high-permeable and low-permeable facies, respectively, following Gershenzon et al. (Gershenzon et al., 2015). S_{gr} is the residual gas saturation, which was assigned as 0 for the drainage curve and as S_{gr-max} for the boundary imbibition curve (Fig. 3A). In Eclipse 300 simulation, Killough's hysteresis model was selected to calculate the history-dependent imbibition curve for non-wetting phase, i.e., the relative permeability hysteresis.

For capillary pressure, the Brooks-Corey relation was used to calculate the drainage curves (Brooks and Corey, 1966):

$$P_c=P_e\left(\frac{S-S_{wi}}{1-S_{wi}}\right)^{-1/\lambda} \quad (7)$$

where P_e is the capillary entry pressure, and λ is the pore-size distribution index for the Brooks-Corey model.

For high-permeable facies, P_e and λ were assigned values of 0.046 bar and 0.55, respectively, following Krevor et al. (Krevor et al., 2012). For low-permeable, P_e was scaled based on the Leverett J-function as proposed by Saadatpoor et al. (Saadatpoor et al., 2010):

$$P_e^{nr}=P_e^{r}\left(\frac{k^{nr}\times\Phi^{r}}{k^{r}\times\Phi^{nr}}\right)^{-0.5} \quad (8)$$

where the superscripts of r and nr represent high-permeable and low-permeable facies, respectively. For imbibition process, a curve analog to drainage was used as the boundary imbibition curve, following Gershenzon et al. (2015). For each facies, the imbibition curve and the drainage curve cross the saturation axis at $S=1-S_{gr\text{-}max}$ and $S=1$, respectively, while their other segments are the same. (Fig. 3B).

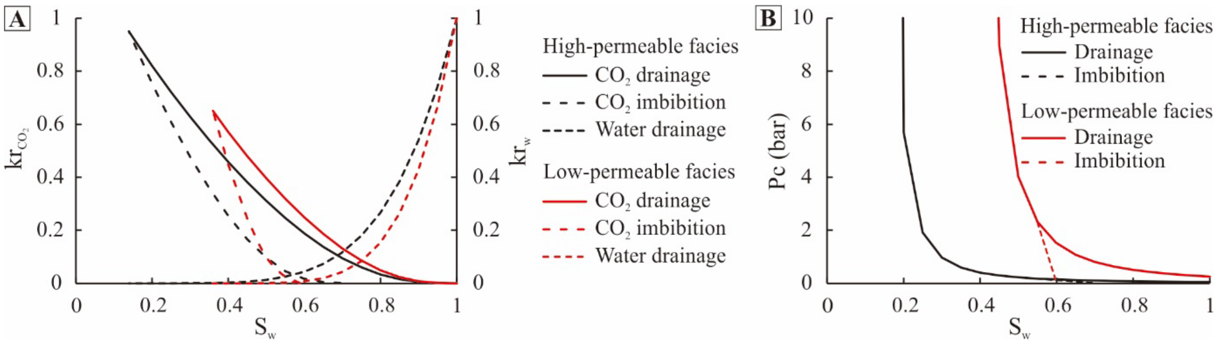

Fig. 3. (A) Relative permeability curves and (B) capillary pressure curves (versus water saturation) for drainage and boundary imbibition processes of high-permeable and low-permeable facies.

In the Eclipse 300 simulations, the water compressibility was assigned a value of 4.35×10^{-5} bar^{-}, following Gershenzon et al. (Gershenzon et al., 2017c). Three components are included in the simulations, i.e., H_2O, CO_2 and NaCl with the initial mole fractions of 0.95, 0 and 0.05, respectively. The mutual solubility of H_2O and CO_2 was obtained based on fugacity equilibration between water and CO_2, following the method proposed by Spycher and Pruess (Spycher and Pruess, 2005). The water diffusion coefficients for all components are 0.0001, and the gas diffusion coefficients for water and CO_2 are 0.001, following Gershenzon et al. (Gershenzon et al., 2017c). The initial reservoir temperature and the equilibrium pressure at a datum depth of 2,000 m are 80°C and 250 bar, respectively. For CO_2 injection, a vertical injection well is located in the model center (model cells: 25, 25, 0 to 25, 25, 50), and is open in the lower half (model cells: 25, 25, 26 to 25, 25, 50). The maximum injection rate of CO_2 is 5.48×10^{5} kg/day, and the default value of the maximum bottom hole pressure is 600 bar in the CO2STORE option. The injection stage is ten years with the maximum total mass of injected CO_2 of two million tons (Mt), followed by the one-hundred-year post-injection period. For boundary conditions, the top and bottom boundaries and the peripheral sides were set as no-flow boundaries to represent a close system. However, the injected CO_2 has not crossed or even approached the peripheral boundaries. This indicates that the model domain is large enough that the peripheral boundary conditions do not significantly affect CO_2 migration.

Table 2 Key physical, geometric and injection parameters used for reservoir simulation.

	Simulation parameters	High-permeable facies	Low-permeable facies
Variable parameters	Average porosity, Φ	0.25	0.15
	Average permeability, k (mD)	661.05	6.73
	Average irreducible water saturation, S_{wi}	0.139	0.360
	Maximum residual gas saturation, $S_{gr\text{-}max}$	0.305	0.402
	CO_2 relative permeability at S_{wi}, $K_{rg}(S_{wi})$	0.95	0.65
	Entry pressure, Pe (bar)	0.046	0.255
Constant parameters	Pore size distribution index, λ	0.55	
	Water compressibility (bar^{-})	4.35×10^{-5}	
	Initial component, $H_2O/CO_2/NaCl$	0.95/0/0.05	
	Aquifer depth (m)	2000	
	Aquifer temperature (°C)	80	
	Aquifer pressure (bar)	250	
	Injection fluid	CO_2	
	Maximum injection rate (kg/day)	5.48×10^{5}	
	Maximum bottom hole pressure (bar)	600	
	Injection stage (years)	10	
	Post-injection period (years)	100	
	Model size (m^3)	5000×5000×50	
	Model discretization (m^3)	100×100×1	

3.3. Selection of optimal lithofacies associations for CO_2 storage

Multi-criteria decision-making (MCDM) deals with finding results in complex scenarios including conflicting objectives and criteria (Kumar et al., 2017), which has been applied to different aspects of the CCS chain, such as barrier analysis (Sara et al., 2015) and site selection for CO_2 storage (Llamas and Cienfuegos, 2012; Alcalde et al., 2021; Sun et al., 2021a). In this study, the MCDM method called the Technique for Order of Preference by Similarity to Ideal Solution (TOPSIS) was used to quantify the overall suitability of different lithofacies associations for CO_2 storage. Four aspects (six criteria) of CO_2 storage were included in this assessment, including ratio of theoretical storage volume, injectivity (average bottom hole pressure, total mass of injected CO_2), distribution (proportion of cells percolated by injected CO_2, proportion of injected CO_2 reaching the top model layer), and phases (proportion of free CO_2) of CO_2. An ideal lithofacies association should have a large storage volume, a low bottom hole pressure, a large mass of injected CO_2, a large proportion of percolated cells, a low proportion of CO_2 in the top model layer, and a low proportion of free CO_2. All parameters were normalized and weighted based on the following method:

$$Y_{ij}=\frac{X_{ij}\times W_j}{\sqrt{\sum_{i=1}^{n}X_{ij}^2}} \quad (9)$$

where Y is the normalized and weighted value, X is the actual value, W is the weighting of each criterion, and i and j are the number of model scenarios and criteria, respectively. In this study, an equal weighting scenario was applied when assessing the suitability of different lithofacies associations, i.e., 0.25 of weighting for storage capacity, injectivity, distribution and CO_2 phases, respectively. Certainly, the criteria can be unequally considered using different weightings based on practical conditions in different projects and studies. A pair of positive and negative ideal solutions were hypothesized based on the best and worst values for each criterion. Finally, the distances between each model scenario to the positive (d_+) and negative (d_-) ideal solutions were calculated, which were used to calculate the TOPSIS score (T_s) (Fig. 4 from Sun et al. (Sun et al., 2021a)):

$$T_s = \frac{d_+}{d_+ + d_-} \quad (10)$$

The model scenario with the minimum TOPSIS score will be selected as the optimal lithofacies association for CO_2 storage.

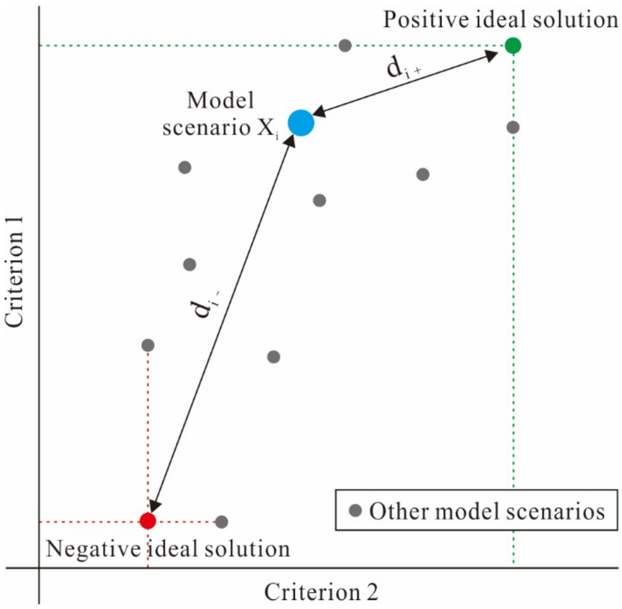

Fig. 4. Adapted scheme of the Technique for Order Preference by Similarity to Ideal Solution (TOPSIS) method (Yoon and Hwang, 1995), from Sun et al. (2021a). Model scenarios are defined in a multidimensional space determined by their values in each criterion. The best and worst values of the models in each criterion determine the positive and negative ideal solutions, respectively. The distances to the positive (d_{i+}) and negative (d_{i-}) ideal solutions are combined into a TOPSIS score (T_s).

4. Results

4.1. Reservoir models and storage volume

From model scenarios 1 to 11, facies models present a decreasing fraction, thickness and width and increasing tortuosity of high-permeable facies (fluvial channel deposits) and an increasing fraction and size of low-permeable facies (overbank deposits). As shown in Fig. 5A, model scenario 3 can represent the LAp in Fig. 2B, and is dominated by thick, wide and well-connected high-permeable facies (⩾80%), resulting in an overall high reservoir quality. In contrast, low-permeable facies present a low fraction (⩽20%), small size, and isolated distribution in this model (Fig. 5A). As shown in Fig. 5C, model scenario 7 can represent the LAmd in Fig. 2E, and consists of major low-permeable facies (⩾60) and minor high-permeable facies (⩽ 40%) causing an overall low reservoir quality. High-permeable facies appear with relatively small size, and are compartmentalized by large low-permeable facies to a great extent (Fig. 5C). Model scenario 5 in Fig. 5B can represent the LApm in Fig. 2D, and shows a moderate fraction, size and connectivity of high-permeable facies between that of the LAp and the LAmd. With a decreasing fraction of high-permeable facies from model scenarios 1 to 11, the ratio of the theoretical storage volume to the total rock volume calculated by the volumetric method gradually reduces from 21.5% to 9.6% (Fig. 6A).

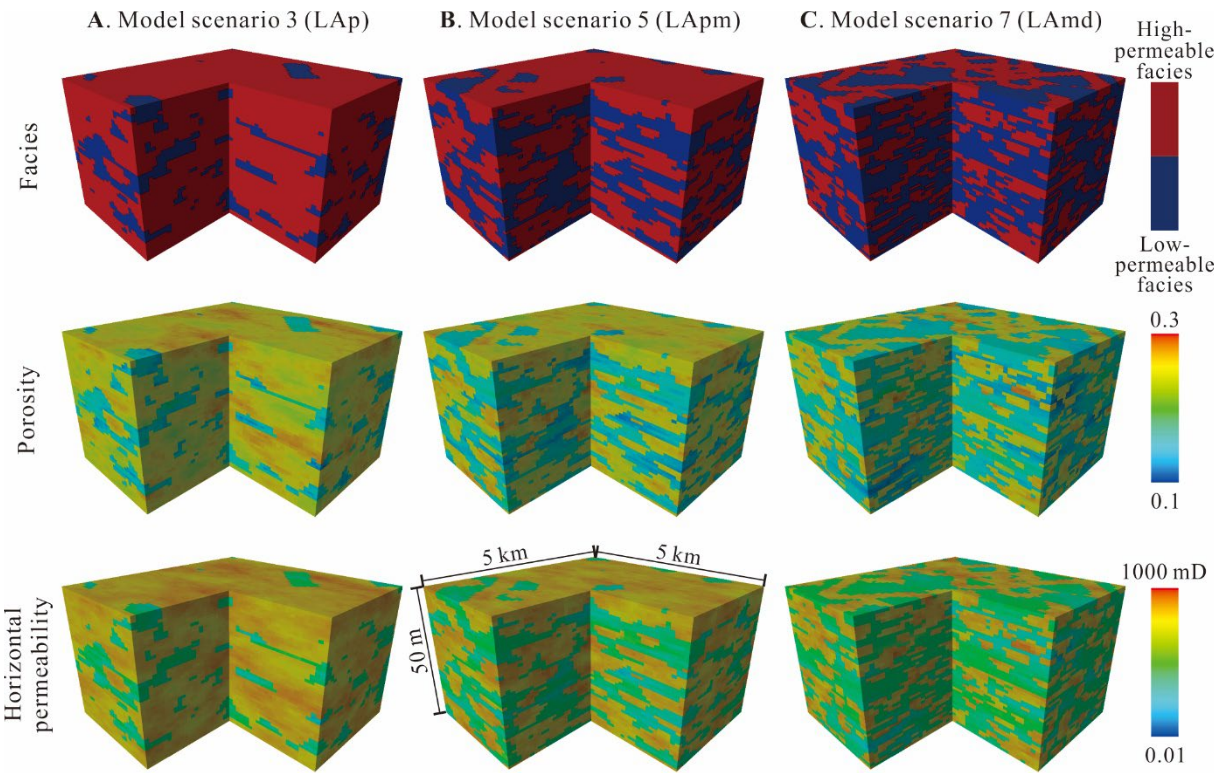

Fig. 5. Reservoir models of typical lithofacies associations: (A) model scenario 3 (high-permeable facies: 80%) – LAp in Fig. 2B; (B) model scenario 5 (high-permeable facies: 60%) – LApm in Fig. 2D; (C) model scenario 7 (high-permeable facies: 40%) – LAmd in Fig. 2E. High-permeable facies consists of fluvial channel deposits, and low-permeable facies consists of overbank deposits.

4.2. CO_2 injectivity

In this study, CO_2 injectivity is analyzed using two proxies, i.e., the bottom hole pressure (BHP) and the total mass of injected CO_2 (Fig. 6B, C). CO_2 injectivity reduces with decreasing permeability, thickness and connectivity of reservoirs. BHP increases with decreasing injectivity, and determines the total mass of injected CO_2 when BPH reaches the upper limit during the injection stage (a default value of 600 bar in Eclipse). From model scenarios 1 to 11, the average BHP presents a gradual increment from 289 to 600 bar due to the declining reservoir quality and connectivity (Fig. 6B). For model scenarios 1 to 7, BHP remains lower than 350 bar, and the average BHP shows a slight increment. For model scenarios 8 and 9, BHP remains lower than 500 bar, but the average BHP increases significantly. In scenarios 1 to 9, CO_2 is injected at the maximum injection rate possible (5.48×10^5 kg of CO_2/day), resulting in the storage of the maximum CO_2 mass available (2 Mt; Fig. 6C). For model scenarios 10 and 11, BHP remains at the upper limit throughout the injection stage (Fig. 6B) due to the very low reservoir quality, causing a significant reduction of the total injected CO_2 to 0.7 Mt and 0.6 Mt, respectively (Fig. 6C). These results indicate that CO_2 injectivity gradually decreases from scenarios 1 to 11 but at a distinct rate.

4.3. CO_2 distribution

CO_2 distribution is analyzed here by studying two aspects of the simulation results: the proportion of cells percolated by the injected CO_2 and the proportion of injected CO_2 reaching the top model layer (Fig. 6D, E). The proportion of swept cells presents an increase from 2.8% to 3.9% in model scenarios 1 to 4, an overall slight reduction in scenarios 4 to 9, and a sharp reduction to 2.2% and 2.0% in scenarios 10 and 11 (Fig. 6D), due to lower mass of injected CO_2 input into the system (Fig. 6C). The proportion of CO_2 reaching the top model layer shows a significant decrease from 20.1% to 0.9% from model scenarios 1 to 4, and remains at low values in scenarios 4 to 9 (Fig. 6E). This proportion increases to 3.0% from scenarios 9 to 11.

As shown in the vertical cross sections and the top horizontal cross sections of CO_2 saturation at the end of the post-injection period, different lithofacies associations present distinct distribution patterns of the injected CO_2 (Fig. 7). For the LAp (Fig. 7A), the CO_2 plume is dominated by vertical migration with limited lateral migration due to the well-connected reservoirs in the vertical direction. Most CO_2 accumulates in the upper half of the model with much CO_2 reaching the top model layer. For the LApm (Fig. 7B), CO_2 migration in the horizontal direction is larger than that of the LAp due to the vertical seepage barriers of low-permeable layers, resulting in a larger CO_2 plume. Most CO_2 maintains in the lower half model with a very small proportion of CO_2 migrating to the top model layer. Compared to the LApm, the LAmd features smaller CO_2 migration in the horizontal direction due to the smaller reservoir size and the weaker lateral connectivity. The LAmd has a smaller CO_2 plume than that of the LApm but a larger plume than that of the LAp (Fig. 7C). Furthermore, most CO_2 maintains in the lower half model, and very limited CO_2 migrates to the top model layer.

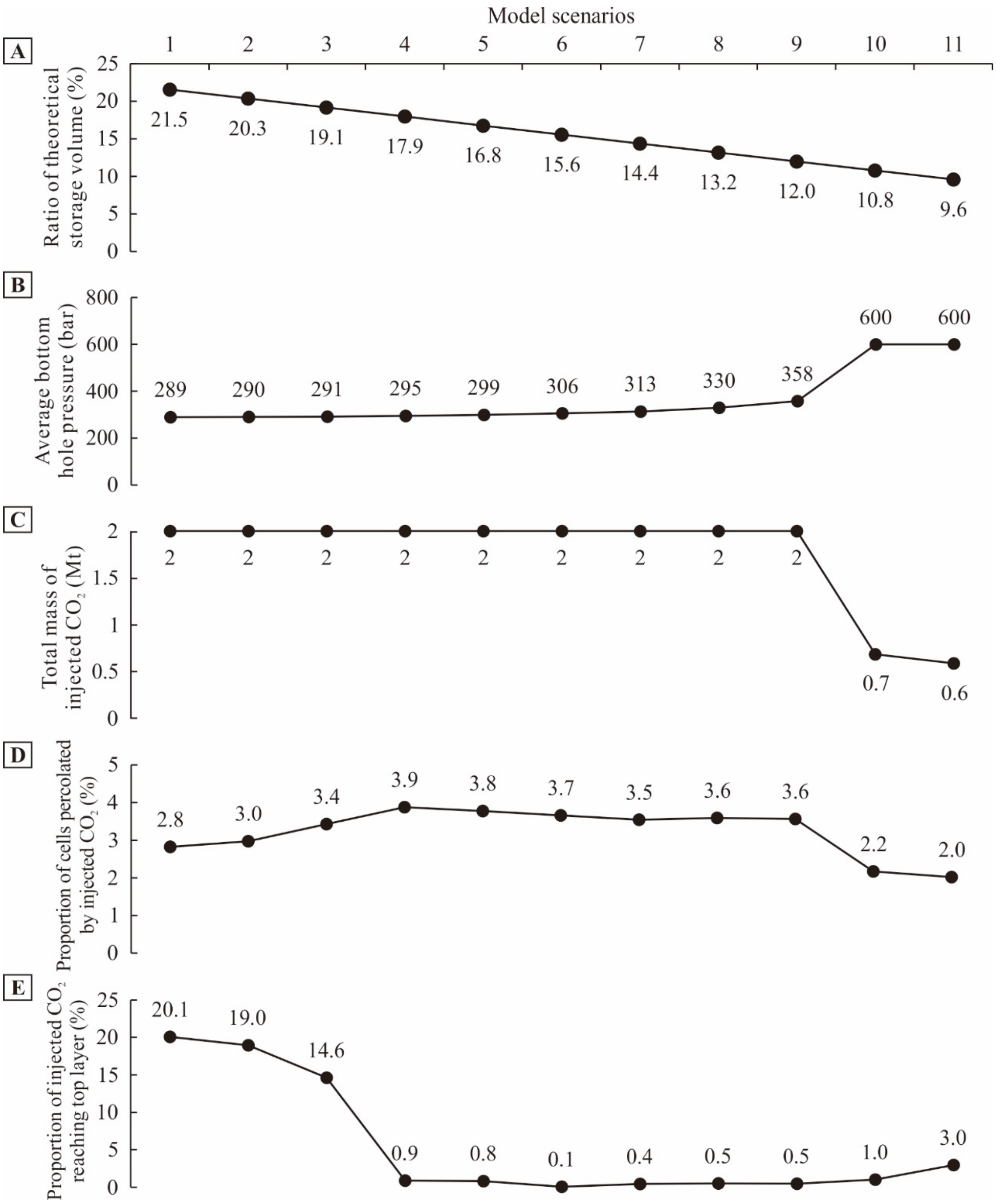

Fig. 6. Simulation results of 11 model scenarios: (A) ratio of theoretical storage volume; (B) average bottom hole pressure; (C) total mass of injected CO_2; (D) proportion of cells percolated by injected CO_2; (E) proportion of injected CO_2 reaching top layer.

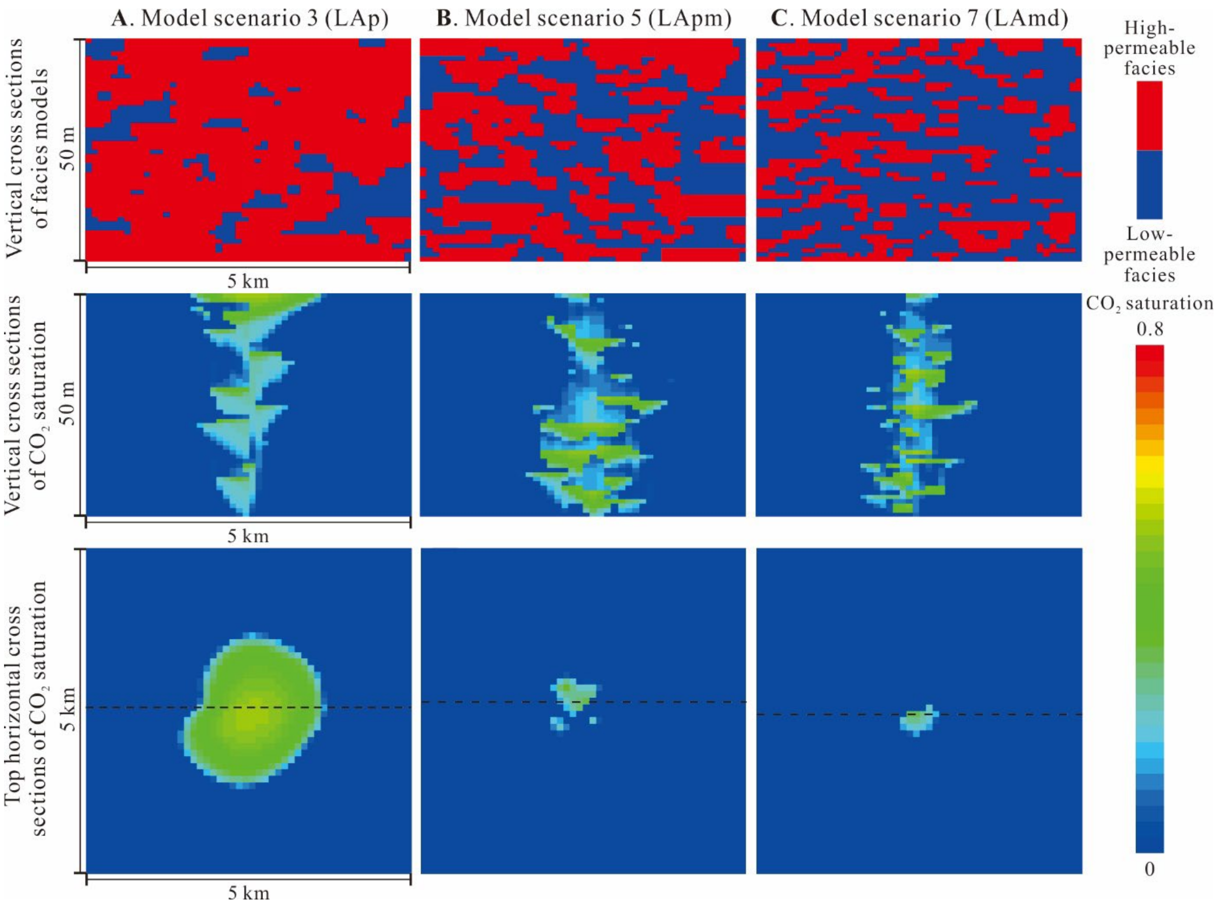

Fig. 7. Vertical cross sections of facies models and their vertical and top horizontal cross sections of CO_2 saturation at the end of the post-injection period: (A) model scenario 3 – LAp; (B) model scenario 5 – LApm; (C) model scenario 7 – LAmd. The vertical facies and saturation cross sections of each model scenario have the same orientation, as shown by the dashed line in the top horizontal cross sections.

4.4. CO_2 phases

CO_2 phase states (free, residual and dissolved phases) vary with time in different model scenarios. Initially, all injected CO_2 is in free phase. During the injection stage (first ten years), free and dissolved CO_2 phases significantly increase over time, while a very small amount of CO_2 occurs as residual phase (Fig. 8). In the early post-injection stage (ten years to around 10,000 days), residually trapped CO_2 increases rapidly while dissolved CO_2 does it slowly, with free CO_2 reducing dramatically. Subsequently, the three CO_2 phases show the similar trends as in the early post-injection stage but at much lower rates for free and residual CO_2 phases. Although most residually trapped CO_2 occurs during the post-injection stage, the small amount of residually trapped CO_2 occurs during the injection stage (Fig. 8). This is mainly because the imbibition process occurs in heterogeneous reservoirs even during the injection period because of different relative permeability characteristics for different facies (Gershenzon et al., 2017b).

The proportions of CO_2 in different phases at the end of the post-injection stage vary in the different model scenarios (Fig. 9). The proportions of free CO_2 decrease to the minimum value of 22.8% from model scenarios 1 to 4, and then increase to the maximum value of 32.2% from scenarios 4 to 8, and finally reduce again in scenarios 9 to 11. From model scenarios 1 to 11, the proportions of residual CO_2 maintain at relatively high values of around 56% in first four scenarios, then present a continuous reduction to the minimum value of 48.0%, and finally an overall increment. The proportions of dissolved CO_2 increase from 14.9% to 21.6% from scenarios 1 to 4. Subsequently, the proportions decrease and remain at around 19.6%, which increase significantly in scenarios 10 and 11. The LAp features relatively high proportions of residual CO_2, low but increasing dissolved CO_2, and thus decreasing free CO_2 with increasing fractions of low-permeable facies (Fig. 9). The LApm presents relatively high proportions of dissolved CO_2, decreasing residual CO_2, and thus increasing free CO_2 with increasing low-permeable facies. The LAmd shows moderate proportions of dissolved CO_2, low residual CO_2, and thus overall high free CO_2.

4.5. Optimal lithofacies association for CO_2 storage

The optimal lithofacies association for CO_2 storage can be selected based on the consideration of the aforementioned four aspects (six criteria), i.e., storage volume (the ratio of theoretical storage volume), CO_2 injectivity (the average BHP, the total mass of injected CO_2), CO_2 distribution (the proportion of cells percolated by injected CO_2, the proportion of injected CO_2 reaching the top model layer), and CO_2 phases (the proportion of free CO_2). Because none of the model scenarios ranks high in all six criteria, the TOPSIS method can be an effective way to quantitatively evaluate the overall suitability of each lithofacies association for CO_2 storage. As shown in Table 3, the TOPSIS scores present first a reduction and then an increment from model scenarios 1 to 11. Model scenarios 4 to 6 with the relatively low TOPSIS scores are the potential lithofacies associations for CO_2 storage. This indicates that the suitability of the LApm for CO_2 storage is higher than that of the LAp, LAmd and LAd lithofacies associations.

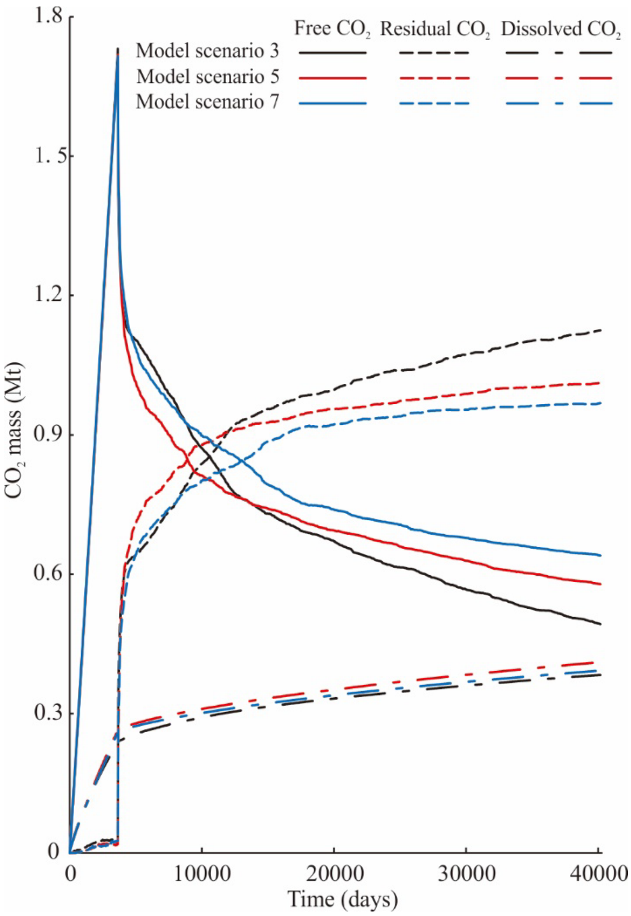

Fig. 8. Evolution of different CO_2 phases over time in model scenarios of typical lithofacies associations.

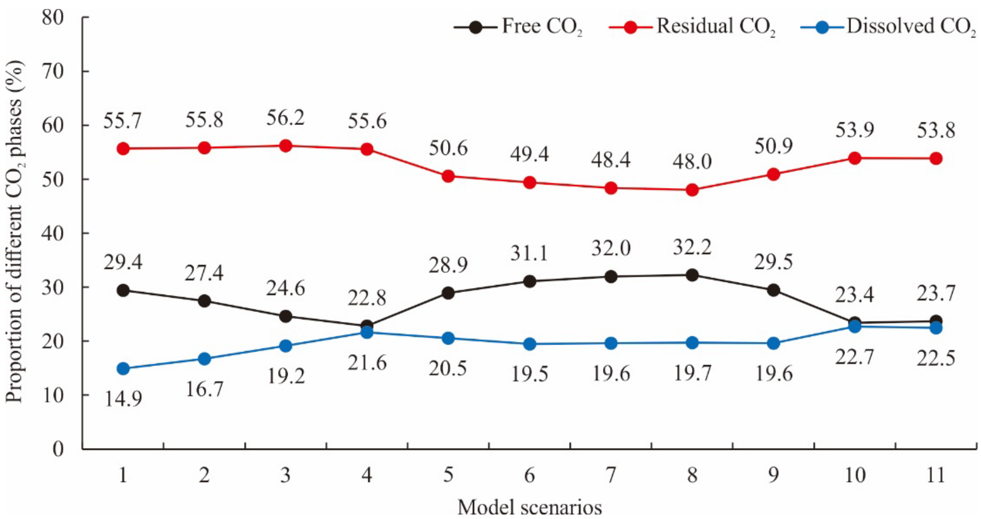

Fig. 9. Proportions of different CO_2 phases at the end of the post-injection period for different model scenarios.

Table 3 Ranking process and TOPSIS results to select the optimal lithofacies association for CO_2 storage.

			Storage volume	CO_2 injectivity		CO_2 distribution		CO_2 phases
		Criteria	Ratio of theoretical storage volume (%)	Average bottom hole pressure (bar)	Total mass of injected CO_2 (Mt)	Proportion of cells percolated by CO_2 (%)	Proportion of CO_2 reaching top layer (%)	Proportion of free CO_2 (%)
Data processing		Weighting	0.25	0.125	0.125	0.125	0.125	0.25
	Actual values / Model scenarios	1	21.53	289	2	2.8	20.1	29.4
		2	20.33	290	2	3.0	19.0	27.4
		3	19.14	291	2	3.4	14.6	24.6
		4	17.95	295	2	3.9	0.9	22.8
		5	16.76	299	2	3.8	0.8	28.9
		6	15.56	306	2	3.7	0.1	31.1
		7	14.37	313	2	3.5	0.4	32.0
		8	13.18	330	2	3.6	0.5	32.2
		9	11.99	358	2	3.6	0.5	29.5
		10	10.79	600	0.7	2.2	1.0	23.4
		11	9.60	600	0.6	2.0	3.0	23.7
	Normalized and weighted values / Model scenarios	1	0.101	0.029	0.041	0.032	0.080	0.079
		2	0.096	0.029	0.041	0.034	0.075	0.074
		3	0.090	0.029	0.041	0.039	0.058	0.066
		4	0.084	0.029	0.041	0.045	0.004	0.062
		5	0.079	0.030	0.041	0.043	0.003	0.078
		6	0.073	0.030	0.041	0.042	0.000	0.084
		7	0.068	0.031	0.041	0.041	0.002	0.086
		8	0.062	0.033	0.041	0.041	0.002	0.087
		9	0.056	0.036	0.041	0.041	0.002	0.079
		10	0.051	0.060	0.014	0.025	0.004	0.063
		11	0.045	0.060	0.012	0.023	0.012	0.064
TOPSIS ranking		Positive ideal solution	0.101	0.029	0.041	0.045	0.000	0.062
		Negative ideal solution	0.045	0.060	0.012	0.023	0.080	0.087
		Ranking result	d+	d-	TOPSIS score	Ranking		
	Model scenarios	1	0.082	0.065	0.558	10		
		2	0.077	0.063	0.550	9		
		3	0.059	0.059	0.500	7		
		4	0.017	0.085	0.168	1		
		5	0.028	0.074	0.275	2		
		6	0.036	0.068	0.346	3		
		7	0.042	0.062	0.403	4		
		8	0.047	0.059	0.445	5		
		9	0.049	0.056	0.465	6		
		10	0.068	0.059	0.536	8		
		11	0.075	0.056	0.570	11		

5. Discussion

Based on the systematic analysis of the storage volume, injectivity, distribution and phases of CO_2, as well as the multi-criteria decision-making assessment results, this section discusses the overall effects of fluvial lithofacies associations on the efficiency of CO_2 storage, and compares our study of the reservoir analog in the Puig-reig anticline with other real projects of CO_2 storage worldwide.

The proximal fluvial lithofacies associations (LAp: model scenarios 1 to 3) present an overall high reservoir quality and connectivity in both the vertical and horizontal directions (Fig. 5A). The advantages of these lithofacies associations for CO_2 storage are the high storage volumes and injectivity (Fig. 6A-C). However, the CO_2 plume is dominated by vertical migration with limited lateral displacement due to the lack of effective seepage barriers in the vertical direction (Fig. 7A). A large proportion of CO_2 (14.6%-20.1%) migrates to the top model layer and is in direct contact with the upper caprocks, which could increase the leakage risk with the accumulating buoyancy force of CO_2 plume. Thus, the storage security in these lithofacies associations depends on the caprock integrity (Espinoza and Santamarina, 2017; Iglauer, 2018). In the LAp, the high vertical reservoir connectivity promotes the vertical migration of the CO_2 plume. Once the CO_2 injection ceases, a large amount of brine imbibes and replaces CO_2 at the plume tail, resulting in relatively high proportions of residual CO_2 in pore spaces than other lithofacies associations (Fig. 9). Moreover, with increasing fractions of low-permeable facies in the LAp (from 0 to 20% in model scenarios 1 to 3), the CO_2 plume is characterized by a wider lateral migration while maintaining the vertical migration, resulting in increasing proportions of model cells percolated by the injected CO_2 (Fig. 6D) and thus higher proportions of dissolved CO_2 (Fig. 9). Therefore, the high proportions of residual CO_2 and increasing proportions of dissolved CO_2 result in the overall decreasing proportions of free CO_2 from scenarios 1 to 3 (29.4% to 24.6%; Fig. 9). As indicated by the TOPSIS ranking results (Table 3), the proximal fluvial lithofacies associations show higher potential for CO_2 storage with increasing portions of low-permeable facies.

The proximal-medial lithofacies associations (LApm: model scenarios 4 to 6) show relatively lower reservoir quality and connectivity than those of the LAp (Fig. 5B). Although these lithofacies associations have lower theoretical storage volumes (Fig. 6A), the CO_2 injectivity to them only shows a very slight reduction (Fig. 6B, C). Due to the seepage barriers in the vertical direction, most of the injected CO_2 stays in the lower half model, with limited CO_2 migrating to the uppermost model layer (0.1% to 0.9%). This indicates that there is a lower leakage risk of CO_2 through caprocks. Compared to the LAp, the LApm features a wider lateral migration while maintaining the vertical migration, resulting in a larger CO_2 plume as shown in Fig. 6D and Fig. 7B. Thus, the LApm is characterized by relatively high proportions of dissolved CO_2 than other lithofacies associations (Fig. 9) due to a larger swept area by CO_2 (Fig. 6D). In the LApm, with increasing fractions of low-permeable facies (from 30% to 50% in model scenarios 4 to 6), dissolved CO_2 decreases due to a slightly reducing swept area. Besides, brine imbibition is restricted at the CO_2 plume tail due to the vertical obstruction of CO_2 migration by the vertical flow barriers, resulting in decreasing residual CO_2. Therefore, the decreasing proportions of dissolved and residual CO_2 together lead to increasing proportions of free CO_2 (22.8% to 31.1%; Fig. 9). In terms of CO_2 distribution and phases, scenario 4 is the most suitable lithofacies association for CO_2 storage. As indicated by the TOPSIS ranking results (Table 3), the proximal-medial fluvial lithofacies show lower potential for CO_2 storage with increasing low-permeable portions.

Compared to the LAp and LApm, the medial-distal lithofacies associations (LAmd: model scenarios 7 to 9) present lower reservoir quality and connectivity (Fig. 5C), resulting in lower theoretical storage volume and injectivity. Although very limited CO_2 migrates to the top model layer (0.4%-0.5%), the relatively high injection pressure could potentially damage the well integrity (Bai et al., 2016; Gholami et al., 2021) and the rock integrity (Rutqvist et al., 2008; Li et al., 2022), which would result in a leakage risk increase. The LAmd features high fractions of low-permeable facies and thus low vertical and lateral reservoir connectivity. In the LAmd, the vertical obstruction of CO_2 migration caused by the flow barriers leads to relatively weak brine imbibition and thus low proportions of residual CO_2. Besides, the slightly smaller swept area of CO_2 results in the overall lower dissolved CO_2 than that of the LApm. These together lead to relatively high proportions of free CO_2 (29.5%-32.2%; Fig. 9). As indicated by the TOPSIS ranking (Table 3), the proximal-medial fluvial lithofacies show lower potential for CO_2 storage with increasing non-reservoir portions.

Based on the above analyses, the LApm (especially with an appropriate fraction of low-permeable facies ranging from 30% to 40%) would be the more promising targets for CO_2 storage compared to the LAp and LAmd lithofacies associations in fluvial systems. Although simulation results can slightly vary using different simulation scenarios, such as different CO_2 injection scenarios or seepage parameters, the take-home message is that the effects of heterogeneous fluvial reservoir architectures on the efficiency of CO_2 geological storage are not monotonic but variable, and that reservoirs with moderate heterogeneous architectures can be beneficial for CO_2 storage.

As one of the main deposit systems of clastic sediments, especially at the margins of non-marine foreland basins, fluvial fans are widely developed worldwide (Horton and Decelles, 2001; Ventra and Clarke, 2018). Many candidate reservoirs for CO_2 geological storage are located in reservoir systems characterized by fluvial sediments. Several real projects have been deployed in these fluvial sequences, such as the Frio Project (the Frio Formation) (Hovorka et al., 2006), the Cranfield Project (the Tuscaloosa Formation) (Soltanian et al., 2019) and the Decatur Project (the Mount Simon Sandstone) in the United States (Finley, 2014), as well as the CO2CRC Otway Project (the Waarre Formation) in Australia (Dance, 2013). These fluvial deposits tend to present heterogeneous reservoir architectures at multiple scales, which exert significant effects on CO_2 storage. In terms of small-scale fluvial stratigraphic architectures, such as cross-bedding, previous studies demonstrated that this reservoir architecture affects the distribution and phases of the injected CO_2, especially residual and dissolved phases (Gershenzon et al., 2015, 2016, 2017a, 2017b, 2017c, Ershadnia et al., 2020, 2021). For large-scale fluvial stratigraphic architectures, several works documented that reservoir architectures control the storage capacity of CO_2 (Issautier et al., 2014, 2016; Vo Thanh et al., 2020). Focusing on varied fluvial lithofacies associations, this study demonstrates that varied lithofacies associations not only control the storage capacity of CO_2 but also the distribution and phases of the injected CO_2, thus the safety of CO_2 storage. Although the increasing fractions of non-reservoir layers can result in decreasing storage volumes and injectivity of CO_2, they can prevent the direct contact between the CO_2 plume and caprocks and reduce the proportions of free CO_2 phase under certain circumstances, thus reducing the leakage risks of the injected CO_2. Previous studies and our works imply that static and dynamic modeling approaches integrating multiscale architectures of fluvial reservoirs are required for future assessments of such systems.

Heterogeneous reservoir architectures are not only present in fluvial deposition systems, but also in other clastic rocks and carbonate rocks, and thus affect the efficiency of CO_2 storage in these reservoir systems. For example, in the Sleipner Project operating since 1996, the first commercial CO_2 storage project, more than 20 Mt of CO_2 has been injected into the Utsira Sand (Global CCS Institute, 2020). These deposits were deposited in marine environments, i.e., turbidite fans or shallow shelfs (Chadwick et al., 2004). The Utsira Sand is dominated by high-quality sandstone reservoirs with limited thin mudstone layers (generally around one meter except for a single 5 m thick layer close to the reservoir top) (Chadwick et al., 2004). Due to the existence of thin mudstone layers, the CO plume generally presents laterally extensive accumulations under seepage barriers, which are clearly shown by time-lapse (4D) seismic profiles (Chadwick et al., 2005; Ghosh et al., 2015). However, the erosion or faulting causes the local absence of the seepage barriers and result in the remigration of the accumulated CO_2 to the thick mudstone layer and even the reservoir top (Zweigel et al., 2004). Thus, the small number of mudstone layers can improve the lateral migration of the CO_2 plume and delay the time for the injected CO_2 to reach the reservoir top to a small extent, which is similar to the situation of proximal fluvial lithofacies associations in this study. In summary, the effect of the mudstone seepage barriers on the efficiency of CO_2 storage depends on the fraction and distribution of the mudstone layers. This study provides a methodology and process for selecting the optimal lithofacies associations for CO_2 storage.

6. Conclusions

Reservoirs of fluvial origins are characterized by heterogeneous stratigraphic architectures at different scales. The fluvial sedimentary heterogeneities not only control the CO_2 storage capacity but also provide clues about the safety of CO_2 storage. Based on a multidisciplinary approach that integrates a field-based sedimentology study, static reservoir modeling, and numerical simulation of CO_2 injection, the overall effects of variable fluvial lithofacies associations on the efficiency of CO_2 storage of a fluvial reservoir analog at the Puig-reig anticline in the SE Pyrenees (Spain) has been evaluated. The proximal fluvial lithofacies associations are dominated by large channel-filling reservoirs with limited overbank non-reservoir deposits. These associations are characterized by a large theoretical storage volume, good reservoir injectivity, and an overall low fraction of free CO_2. However, a high fraction of CO_2 would quickly migrate toward the reservoir tops in direct contact with the top seal, increasing the leakage risk. The medial-distal fluvial lithofacies associations consist of interbedded reservoir bodies and non-reservoir barriers, with much lower reservoir fractions. These associations can significantly hinder the upward migration of CO_2, preventing it from reaching the reservoir tops. However, they feature a low theoretical storage volume, low reservoir injectivity, and a relatively high fraction of free CO_2. The proximal-medial fluvial lithofacies associations with moderately heterogeneous architecture are better suited for CO_2 storage, when considering the storage volume, injectivity, distribution and phases of CO_2 comprehensively.

The heterogeneous architectures of fluvial reservoirs can exert significant but variable effects on the efficiency of CO_2 storage. Although the specific values of static and dynamic modeling results could potentially change according to different geological settings or simulation scenarios, it is concluded that reservoirs with moderate heterogeneous architectures appear to be better targets for CO_2 geological storage compared with homogenous reservoirs. When selecting CO_2 storage sites, it is recommended that reservoir quality, caprock integrity and heterogeneous reservoir architectures should all be considered.

CRediT authorship contribution statement

Xiaolong Sun: Conceptualization, Methodology, Software, Investigation, Writing – original draft. **Yingchang Cao:** Supervision, Writing – review & editing, Project administration. **Keyu Liu:** Supervision, Writing – review & editing, Project administration. **Juan Alcalde:** Supervision, Conceptualization, Methodology, Validation. **Patricia Cabello:** Methodology, Software. **Anna Travé:** Supervision, Validation, Project administration. **David Cruset:** Validation. **Enrique Gomez-Rivas:** Supervision, Conceptualization, Methodology, Validation.

Declaration of Competing Interest

The authors declare that they have no known competing financial interests or personal relationships that could have appeared to influence the work reported in this paper.

Data availability

The data that support the findings of this study are available from the corresponding author upon reasonable request.

Acknowledgments

Funding was provided by the China University of Petroleum (East China) to the Independent Innovation Research Project 22CX06004A and by the Catalan Council to the Grup Consolidat de Recerca "Geologia Sedimentària" (2017SGR-824) and the DGICYT Spanish Projects PGC2018-093903-B-C22, PID2020-118999GB-I00 and PID2021-122467NB-C22 (MCIN/ AEI/ 10.13039/501100011033/ FEDER, Unión Europea). JA acknowledges funding from MICINN (Juan de la Cierva fellowship - IJC2018-036074-I). DC acknowledges MCIN/AEI /10.13039/501100011033 and European Union NextGenerationEU/PRTR (Juan de la Cierva Formación fellowship FJC2020-043488-I). EGR acknowledges funding from MCIN ("Ramón y Cajal" fellowship RYC2018-026335-I). PC acknowledges funding from the research project RTI2018-097312-A-I00 financed by MCIN/ AEI/ 10.13039/501100011033/ FEDER "Una manera de hacer Europa" and Grup de Recerca Consolidat de Geodinàmica i Anàlisi de Conques (GGAC), financed by the Generalitat de Catalunya (2017SGR596). This article also benefited from an academic license of Petrel E&P Software Platform and Eclipse 300 from Schlumberger.

References

Abbaszadeh, M., Shariatipour, S., Ifelebuegu, A., 2020. The influence of temperature on wettability alteration during CO_2 storage in saline aquifers. Int. J. Greenh. Gas Control 99, 103101. https://doi.org/10.1016/j.ijggc.2020.103101

Al-Khdheeawi, E.A., Vialle, S., Barifcani, A., Sarmadivaleh, M., Iglauer, S., 2018. Enhancement of CO_2 trapping efficiency in heterogeneous reservoirs by water-alternating gas injection. Greenh. Gases Sci. Technol. 8, 920–931.

Al-Khdheeawi, E.A., Vialle, S., Barifcani, A., Sarmadivaleh, M., Iglauer, S., 2017a. Influence of injection well configuration and rock wettability on CO_2 plume behaviour and CO_2 trapping capacity in heterogeneous reservoirs. J. Nat. Gas Sci. Eng. 43, 190–206.

Al-Khdheeawi, E.A., Vialle, S., Barifcani, A., Sarmadivaleh, M., Iglauer, S., 2017b. Impact of reservoir wettability and heterogeneity on CO_2-plume migration and trapping capacity. Int. J. Greenh. Gas Control 58, 142–158.

Alcalde, J., Flude, S., Wilkinson, M., Johnson, G., Edlmann, K., Bond, C.E., Scott, V., Gilfillan, S.M.V., Ogaya, X., Haszeldine, R.S., 2018. Estimating geological CO_2 storage security to deliver on climate mitigation. Nat. Commun. 9, 2201. https://doi.org/10.1038/s41467-018-04423-1

Alcalde, J., Heinemann, N., James, A., Bond, C.E., Ghanbari, S., Mackay, E.J., Haszeldine, R.S., Faulkner, D.R., Worden, R.H., Allen, M.J., 2021a. A criteria-driven approach to the CO_2 storage site selection of East Mey for the acorn project in the North Sea. Mar. Pet. Geol. 133, 105309. https://doi.org/10.1016/j.marpetgeo.2021.105309

Alcalde, J., Heinemann, N., Mabon, L., Worden, R.H., de Coninck, H., Robertson, H., Maver, M., Ghanbari, S., Swennenhuis, F., Mann, I., Walker, T., Gomersal, S., Bond, C.E., Allen, M.J., Haszeldine, R.S., James, A., Mackay, E.J., Brownsort, P.A., Faulkner, D.R., Murphy, S., 2019. Acorn: Developing full-chain industrial carbon capture and storage in a resource- and infrastructure-rich hydrocarbon province. J. Clean. Prod. 233, 963–971.

Ambrose, W.A., Lakshminarasimhan, S., Holtz, M.H., Núñez-López, V., Hovorka, S.D., Duncan, I., 2008. Geologic factors controlling CO_2 storage capacity and permanence: case studies based on experience with heterogeneity in oil and gas reservoirs applied to CO_2 storage. Environ. Geol. 54, 1619–1633.

Bachu, S., Bonijoly, D., Bradshaw, J., Burruss, R., Holloway, S., Christensen, N.P., Mathiassen, O.M., 2007. CO_2 storage capacity estimation: Methodology and gaps. Int. J. Greenh. Gas Control 1, 430–443.

Bai, M., Zhang, Z., Fu, X., 2016. A review on well integrity issues for CO_2 geological storage and enhanced gas recovery. Renew. Sustain. Energy Rev. 59, 920–926.

Barrier, L., Proust, J.N., Nalpas, T., Robin, C., Guillocheau, F., 2010. Control of alluvial sedimentation at foreland-basin active margins: A case study from the northeastern Ebro Basin (southeastern Pyrenees, Spain). J. Sediment. Res. 80, 728–749.

Brooks, R.H., Corey, A.T., 1966. Properties of porous media affecting fluid flow. J. Irrig. Drain. Div. 92, 61–88.

Budinis, S., Krevor, S., Dowell, N. Mac, Brandon, N., Hawkes, A., 2018. An assessment of CCS costs, barriers and potential. Energy Strateg. Rev. 22, 61–81.

Bui, M., Adjiman, C.S., Bardow, A., Anthony, E.J., Boston, A., Brown, S., Fennell, P.S., Fuss, S., Galindo, A., Hackett, L.A., Hallett, J.P., Herzog, H.J., Jackson, G., Kemper, J., Krevor, S., Maitland, G.C., Matuszewski, M., Metcalfe, I.S., Petit, C., Puxty, G., Reimer, J., Reiner, D.M., Rubin, E.S., Scott, S.A., Shah, N., Smit, B., Trusler, J.P.M., Webley, P., Wilcox, J., Mac Dowell, N., 2018. Carbon capture and storage (CCS): the way forward. Energy Environ. Sci. 11, 1062–1176.

Chadwick, R.., Zweigel, P., Gregersen, U., Kirby, G.., Holloway, S., Johannessen, P.., 2004. Geological reservoir characterization of a CO_2 storage site: The Utsira Sand, Sleipner, northern North Sea. Energy 29, 1371–1381.

Chadwick, R.A., Arts, R., Eiken, O., 2005. 4D seismic quantification of a growing CO_2 plume at Sleipner, North Sea. Geol. Soc. London, Pet. Geol. Conf. Ser. 6, 1385–1399.

Class, H., Ebigbo, A., Helmig, R., Dahle, H.K., Nordbotten, J.M., Celia, M.A., Audigane, P., Darcis, M., Ennis-King, J., Fan, Y., Flemisch, B., Gasda, S.E., Jin, M., Krug, S., Labregere, D., Naderi Beni, A., Pawar, R.J., Sbai, A., Thomas, S.G., Trenty, L., Wei, L., 2009. A benchmark study on problems related to CO_2 storage in geologic formations. Comput. Geosci. 13, 409–434.

Cruset, D., Cantarero, I., Travé, A., Vergés, J., John, C.M., 2016. Crestal graben fluid evolution during growth of the Puig-reig anticline (South Pyrenean fold and thrust belt). J. Geodyn. 101, 30–50.

Dance, T., 2013. Assessment and geological characterisation of the CO2CRC Otway Project CO_2 storage demonstration site: From prefeasibility to injection. Mar. Pet. Geol. 46, 251–269.

De Silva, P.N.K., Ranjith, P.G., 2012. A study of methodologies for CO_2 storage capacity estimation of saline aquifers. Fuel 93, 13–27.

Dullien, F.A.L., 1992. Porous Media Fluid Transport and Pore Structure. Academic Press, San Diego, USA.

Ershadnia, R., Hajirezaie, S., Amooie, A., Wallace, C.D., Gershenzon, N.I., Hosseini, S.A., Sturmer, D.M., Ritzi, R.W., Soltanian, M.R., 2021. CO_2 geological sequestration in multiscale heterogeneous aquifers: Effects of heterogeneity, connectivity, impurity, and hysteresis. Adv. Water Resour. 151, 103895. https://doi.org/10.1016/j.advwatres.2021.103895

Ershadnia, R., Wallace, C.D., Hajirezaie, S., Hosseini, S.A., Nguyen, T.N., Sturmer, D.M., Dai, Z., Reza

Soltanian, M., 2022. Hydro-thermo-chemo-mechanical modeling of carbon dioxide injection in fluvial heterogeneous aquifers. Chem. Eng. J. 431, 133451. https://doi.org/10.1016/j.cej.2021.133451

Ershadnia, R., Wallace, C.D., Soltanian, M.R., 2020. CO_2 geological sequestration in heterogeneous binary media: Effects of geological and operational conditions. Adv. Geo-Energy Res. 4, 392–405.

Espinoza, D.N., Santamarina, J.C., 2017. CO_2 breakthrough—caprock sealing efficiency and integrity for carbon geological storage. Int. J. Greenh. Gas Control 66, 218–229.

Finley, R.J., 2014. An overview of the Illinois Basin - Decatur Project. Greenh. Gases Sci. Technol. 4, 571–579.

Friend, P.F., Sinha, R., 1993. Braiding and meandering parameters. Geol. Soc. London, Spec. Publ. 75, 105–111.

Gershenzon, N.I., Ritzi, R.W., Dominic, D.F., Mehnert, E., 2017a. Effective constitutive relations for simulating CO_2 capillary trapping in heterogeneous reservoirs with fluvial sedimentary architecture. Geomech. Geophys. Geo-Energy Geo-Resources 3, 265–279.

Gershenzon, N.I., Ritzi, R.W., Dominic, D.F., Mehnert, E., Okwen, R.T., 2017b. Capillary trapping of CO_2 in heterogeneous reservoirs during the injection period. Int. J. Greenh. Gas Control 59, 13–23.

Gershenzon, N.I., Ritzi, R.W., Dominic, D.F., Mehnert, E., Okwen, R.T., Patterson, C., 2017c. CO_2 trapping in reservoirs with fluvial architecture: Sensitivity to heterogeneity in permeability and constitutive relationship parameters for different rock types. J. Pet. Sci. Eng. 155, 89–99.

Gershenzon, N.I., Ritzi, R.W., Dominic, D.F., Soltanian, M., Mehnert, E., Okwen, R.T., 2015. Influence of small-scale fluvial architecture on CO_2 trapping processes in deep brine reservoirs. Water Resour. Res. 51, 8240–8256.

Gershenzon, N.I., Ritzi Jr., R.W., Dominic, D.F., Mehnert, E., Okwen, R.T., 2016. Comparison of CO_2 trapping in highly heterogeneous reservoirs with Brooks-Corey and van Genuchten type capillary pressure curves. Adv. Water Resour. 96, 225–236.

Gholami, R., Raza, A., Iglauer, S., 2021. Leakage risk assessment of a CO_2 storage site: A review. Earth-Science Rev. 223, 103849. https://doi.org/10.1016/j.earscirev.2021.103849

Ghosh, R., Sen, M.K., Vedanti, N., 2015. Quantitative interpretation of CO_2 plume from Sleipner (North Sea), using post-stack inversion and rock physics modeling. Int. J. Greenh. Gas Control 32, 147–158.

Gibling, M.R., 2006. Width and Thickness of fluvial channel bodies and valley fills in the geological record: A literature compilation and classification. J. Sediment. Res. 76, 731–770.

Global CCS Institute, 2020. CCS Facilities Database [WWW Document]. URL https://co2re.co/FacilityData (accessed 7.11.22).

Global CCS Institute, 2018. The Global Status of CCS: 2018. [WWW Document]. URL file:///C:/Windows/Temp/global-status-ccs-2015-summary (1).pdf (accessed 2.17.21).

Han, W.S., Lee, S.-Y., Lu, C., McPherson, B.J., 2010. Effects of permeability on CO_2 trapping mechanisms and buoyancy-driven CO_2 migration in saline formations. Water Resour. Res. 46. https://doi.org/10.1029/2009WR007850

Holtz, M.H., 2002. Residual gas saturation to aquifer influx: A calculation method for 3-D computer reservoir model construction, in: SPE Gas Technology Symposium. Society of Petroleum Engineers, Calgary, Canada. https://doi.org/10.2118/75502-MS

Horton, B.K., Decelles, P.G., 2001. Modern and ancient fluvial megafans in the foreland basin system of the Central Andes, Southern Bolivia: Implications for drainage network evolution in foldthrust belts. Basin Res. 13, 43–63.

Hovorka, S.D., Benson, S.M., Doughty, C., Freifeld, B.M., Sakurai, S., Daley, T.M., Kharaka, Y.K., Holtz, M.H., Trautz, R.C., Nance, H.S., Myer, L.R., Knauss, K.G., 2006. Measuring permanence of CO_2 storage in saline formations: the Frio experiment. Environ. Geosci. 13, 105–121.

Iglauer, S., 2018. Optimum storage depths for structural CO_2 trapping. Int. J. Greenh. Gas Control 77, 82–87.

IPCC, 2018. Global Warming of 1.5°C: An IPCC special report [WWW Document]. Intergov. Panel Clim. Chang. URL https://www.ipcc.ch/sr15/ (accessed 7.11.22).

Issautier, B., Viseur, S., Audigane, P., Chiaberge, C., Le Nindre, Y.-M., 2016. A new approach for evaluating the impact of fluvial type heterogeneity in CO_2 storage reservoir modeling. Comptes Rendus Geosci. 348, 531–539.

Issautier, B., Viseur, S., Audigane, P., le Nindre, Y.-M., 2014. Impacts of fluvial reservoir heterogeneity on connectivity: Implications in estimating geological storage capacity for CO_2. Int. J. Greenh. Gas Control 20, 333–349.

Kearns, J., Teletzke, G., Palmer, J., Thomann, H., Kheshgi, H., Chen, Y.H., Paltsev, S., Herzog, H., 2017. Developing a consistent database for regional geologic CO_2 storage capacity worldwide. Energy Procedia 114, 4697–4709.

Kou, Z., Wang, H., Alvarado, V., Fred McLaughlin, J., Quillinan, S.A., 2021. Impact of sub-core scale heterogeneity on CO_2/brine multiphase flow for geological carbon storage in the upper Minnelusa sandstones. J. Hydrol. 599. https://doi.org/10.1016/j.jhydrol.2021.126481

Krevor, S.C.M., Pini, R., Li, B., Benson, S.M., 2011. Capillary heterogeneity trapping of CO_2 in a sandstone rock at reservoir conditions. Geophys. Res. Lett. 38. https://doi.org/10.1029/2011GL048239

Krevor, S.C.M., Pini, R., Zuo, L., Benson, S.M., 2012. Relative permeability and trapping of CO_2 and water in sandstone rocks at reservoir conditions. Water Resour. Res. 48, W02532. https://doi.org/10.1029/2011WR010859

Kumar, A., Sah, B., Singh, A.R., Deng, Y., He, X., Kumar, P., Bansal, R.C., 2017. A review of multi criteria decision making (MCDM) towards sustainable renewable energy development. Renew. Sustain. Energy Rev. 69, 596–609.

Leung, D.Y.C., Caramanna, G., Maroto-Valer, M.M., 2014. An overview of current status of carbon dioxide capture and storage technologies. Renew. Sustain. Energy Rev. 39, 426–443.

Li, J., Chen, Z., Feng, Y., Qu, L., Liu, J., Li, W., Dai, M., 2022. Damage of reservoir rock induced by CO_2 injection. Pet. Sci. https://doi.org/10.1016/j.petsci.2022.03.016

Llamas, B., Cienfuegos, P., 2012. Multicriteria decision methodology to select suitable areas for storing CO_2. Energy Environ. 23, 249–264.

Raza, A., Rezaee, R., Gholami, R., Rasouli, V., Bing, C.H., Nagarajan, R., Hamid, M.A., 2015. Injectivity and quantification of capillary trapping for CO_2 storage: A review of influencing parameters. J. Nat. Gas Sci. Eng. 26, 510–517.

Ren, B., Jeong, H., 2018. Influence of injection strategies on local capillary trapping during geological carbon sequestration in saline aquifers. J. CO_2 Util. 27, 441–449.

Riaz, A., Cinar, Y., 2014. Carbon dioxide sequestration in saline formations: Part I—Review of the modeling of solubility trapping. J. Pet. Sci. Eng. 124, 367–380.

Ringrose, P.S., Meckel, T.A., 2019. Maturing global CO_2 storage resources on offshore continental margins to achieve 2DS emissions reductions. Sci. Rep. 9, 17944. https://doi.org/10.1038/s41598-019-54363-z

Romanov, V., Soong, Y., Carney, C., Rush, G.E., Nielsen, B., O'Connor, W., 2015. Mineralization of Carbon Dioxide: A Literature Review. ChemBioEng Rev. 2, 231–256.

Rutqvist, J., Birkholzer, J.T., Tsang, C.-F., 2008. Coupled reservoir–geomechanical analysis of the potential for tensile and shear failure associated with CO_2 injection in multilayered reservoir–caprock systems. Int. J. Rock Mech. Min. Sci. 45, 132–143.

Saadatpoor, E., Bryant, S.L., Sepehrnoori, K., 2010. New trapping mechanism in carbon aequestration. Transp.

Porous Media 82, 3–17.
Sáez, A., Anadón, P., Herrero, M.J., Moscariello, A., 2007. Variable style of transition between Palaeogene fluvial fan and lacustrine systems, southern Pyrenean foreland, NE Spain. Sedimentology 54, 367–390.
Sara, J., Stikkelman, R.M., Herder, P.M., 2015. Assessing relative importance and mutual influence of barriers for CCS deployment of the ROAD project using AHP and DEMATEL methods. Int. J. Greenh. Gas Control 41, 336–357.
Schlumberger, 2018. Manual "ECLIPSE Reservoir Simulation Software, Technical Description." Version 2018.1.
Scott, V., Gilfillan, S., Markusson, N., Chalmers, H., Haszeldine, R.S., 2013. Last chance for carbon capture and storage. Nat. Clim. Chang. 3, 105–111.
Seigo, S.L., Dohle, S., Siegrist, M., 2014. Public perception of carbon capture and storage (CCS): A review. Renew. Sustain. Energy Rev. 38, 848–863.
Shukla, R., Ranjith, P., Haque, A., Choi, X., 2010. A review of studies on CO_2 sequestration and caprock integrity. Fuel 89, 2651–2664.
Soltanian, M.R., Hajirezaie, S., Hosseini, S.A., Dashtian, H., Amooie, M.A., Meyal, A., Ershadnia, R., Ampomah, W., Islam, A., Zhang, X., 2019. Multicomponent reactive transport of carbon dioxide in fluvial heterogeneous aquifers. J. Nat. Gas Sci. Eng. 65, 212–223.
Spycher, N., Pruess, K., 2005. CO_2-H_2O mixtures in the geological sequestration of CO_2. II. Partitioning in chloride brines at 12–100°C and up to 600 bar. Geochim. Cosmochim. Acta 69, 3309–3320.
Sun, X., Alcalde, J., Bakhtbidar, M., Elío, J., Vilarrasa, V., Canal, J., Ballesteros, J., Heinemann, N., Haszeldine, S., Cavanagh, A., Vega-Maza, D., Rubiera, F., Martínez-Orio, R., Johnson, G., Carbonell, R., Marzan, I., Travé, A., Gomez-Rivas, E., 2021a. Hubs and clusters approach to unlock the development of carbon capture and storage – Case study in Spain. Appl. Energy 300, 117418. https://doi.org/10.1016/j.apenergy.2021.117418
Sun, X., Alcalde, J., Gomez-Rivas, E., Owen, A., Griera, A., Martín-Martín, J.D., Cruset, D., Travé, A., 2021b. Fluvial sedimentation and its reservoir potential at foreland basin margins: A case study of the Puig-reig anticline (South-eastern Pyrenees). Sediment. Geol. 424, 105993. https://doi.org/10.1016/j.sedgeo.2021.105993
Sun, X., Alcalde, J., Gomez-Rivas, E., Struth, L., Johnson, G., Travé, A., 2020. Appraisal of CO_2 storage potential in compressional hydrocarbon-bearing basins: Global assessment and case study in the Sichuan Basin (China). Geosci. Front. 11, 2309–2321.
Sun, X., Gomez-Rivas, E., Alcalde, J., Martín-Martín, J.D., Ma, C., Muñoz-López, D., Cruset, D., Cantarero, I., Griera, A., Travé, A., 2021c. Fracture distribution in a folded fluvial succession: the Puig-reig anticline (South-eastern Pyrenees). Mar. Pet. Geol. 105169. https://doi.org/10.1016/j.marpetgeo.2021.105169
Sun, X., Gomez-Rivas, E., Cruset, D., Alcalde, J., Muñoz-López, D., Cantarero, I., Martín-Martín, J.D., John, C.M., Travé, A., 2022. Origin and distribution of calcite cements in a folded fluvial succession: The Puig-reig anticline (south-eastern Pyrenees). Sedimentology 69, 2319–2347.
Tcvetkov, P., Cherepovitsyn, A., Fedoseev, S., 2019. Public perception of carbon capture and storage: A state-of-the-art overview. Heliyon 5, e02845. https://doi.org/10.1016/j.heliyon.2019.e02845
UNFCCC, 2022. Nationally Determined Contributions (NDCs) [WWW Document]. United Nations Framew. Conv. Clim. Chang. URL https://www4.unfccc.int/sites/NDCStaging/Pages/All.aspx (accessed 7.11.22).
Ventra, D., Clarke, L.E., 2018. Geology and geomorphology of alluvial and fluvial fans: current progress and research perspectives. Geol. Soc. London, Spec. Publ. 440, 1–21.
Vergés, J., 1993. Estudi geològic del vessant sud del Pirineu oriental i central. Evolució cinemàtica en 3D.

University of Barcelona, Barcelona.

Vo Thanh, H., Sugai, Y., Sasaki, K., 2020. Impact of a new geological modelling method on the enhancement of the CO_2 storage assessment of E sequence of Nam Vang field, offshore Vietnam. Energy Sources, Part A Recover. Util. Environ. Eff. 42, 1499–1512.

Williams, E.A., Ford, M., Vergés, J., Artoni, A., 1998. Alluvial gravel sedimentation in a contractional growth fold setting, Sant Llorenç de Morunys, southeastern Pyrenees. Geol. Soc. London, Spec. Publ. 134, 69–106.

Witte, K., 2021. Social Acceptance of Carbon Capture and Storage (CCS) from Industrial Applications. Sustainability 13, 12278. https://doi.org/10.3390/su132112278

Xu, L., Myers, M., Li, Q., White, C., Zhang, X., 2020. Migration and storage characteristics of supercritical CO2 in anisotropic sandstones with clay interlayers based on X-CT experiments. J. Hydrol. 580, 124239. https://doi.org/10.1016/j.jhydrol.2019.124239

Yang, Z., Chen, Y.-F., Niemi, A., 2020. Gas migration and residual trapping in bimodal heterogeneous media during geological storage of CO_2. Adv. Water Resour. 142, 103608. https://doi.org/10.1016/j.advwatres.2020.103608

Yoon, K.P., Hwang, C.L., 1995. Multiple Attribute Decision Making: An Introduction. Sage Publications, Thousand Oaks, CA.

Zhang, S., DePaolo, D.J., 2017. Rates of CO_2 mineralization in geological carbon storage. Acc. Chem. Res. 50, 2075–2084.

Zhang, S., DePaolo, D.J., Xu, T., Zheng, L., 2013. Mineralization of carbon dioxide sequestered in volcanogenic sandstone reservoir rocks. Int. J. Greenh. Gas Control 18, 315–328.

Zweigel, P., Arts, R., Lothe, A.E., Lindeberg, E.B.G., 2004. Reservoir geology of the Utsira Formation at the first industrial-scale underground CO_2 storage site (Sleipner area, North Sea). Geol. Soc. London, Spec. Publ. 233, 165–180.